A Hybrid FETD-FDTD Method with Nonconforming Meshes

Bao Zhu[1,2], Jiefu Chen[2], Wanxie Zhong[1] and Qing Huo Liu[2,*]

[1] *State Key Laboratory of Structural Analysis for Industrial Equipment,*
Dalian University of Technology, Dalian 116023, P.R. China.
[2] *Department of Electrical and Computer Engineering, Duke University,*
Durham NC 27708, USA.

To the memory of David Gottlieb

Abstract. A quasi non-overlapping hybrid scheme that combines the finite-difference time-domain (FDTD) method and the finite-element time-domain (FETD) method with nonconforming meshes is developed for time-domain solutions of Maxwell's equations. The FETD method uses mixed-order basis functions for electric and magnetic fields, while the FDTD method uses the traditional Yee's grid; the two methods are joined by a buffer zone with the FETD method and the discontinuous Galerkin method is used for the domain decomposition in the FETD subdomains. The main features of this technique is that it allows non-conforming meshes and an arbitrary numbers of FETD and FDTD subdomains. The hybrid method is completely stable for the time steps up to the stability limit for the FDTD method and FETD method. Numerical results demonstrate the validity of this technique.

AMS subject classifications: 65L60, 65L12, 20B40, 83L50

Key words: Finite-element time-domain, finite-difference time-domain, discontinuous Galerkin, domain decomposition, non-conforming mesh.

1 Introduction

The finite-difference time-domain (FDTD) method [1] is an efficient and robust time-domain technique based on a structured grid and is ideal for modeling large homogeneous volumes and regular structures, while the finite-element time-domain (FETD) method [2] is more flexible in geometric modeling because of its unstructured mesh. However, the FETD method is not as popular as the FDTD method because a sparse

*Corresponding author. *Email addresses:* zhubao.dlut@gmail.com (B. Zhu), jiefu.chen@duke.edu (J. Chen), wxzhong@dlut.edu.cn (W. Zhong), qhliu@ee.duke.edu (Q. H. Liu)

matrix solution is required for time stepping, which can become very expensive even for moderate-size problems. Therefore, a hybrid FDTD-FETD method can potentially take advantages of both the flexibility of the FETD method and the efficiency of the FDTD method.

Significant efforts have been reported for hybridization of the FETD method with the FDTD method [3–9, 17, 18]. For example, the hybrid FD/FE methods has been developed to solve Maxwell's equations in the time domain, but a weak instability has been reported [3, 4]. A stable hybrid FDTD/FETD method has been presented by [5]. The FETD method utilized in these hybrid methods is based on the second-order wave equation derived from the original first-order Maxwell's equations with a single variable **E** or **H** [10]. A pyramid element is used to joint the structured FDTD grid with the unstructured FETD mesh [11]. To our knowledge, the mesh between subdomains is required to be conformal in the previous approaches.

To improve efficiency and flexibility, a non-conforming mesh between different subdomains is desirable for simulating multi-scale structures. Furthermore, multiple FETD and FDTD regions are necessary when the number of unknowns becomes large. It is the objective of this work to develop such a hybrid scheme that can allow nonconforming meshes and multiple subdomains similar to the discontinuous Galerkin spectral element time-domain (DG-SETD) method in [12]. To facilitate a non-conforming mesh, the discontinuous Galerkin method [13] would be an appropriate framework for hybridizing the FETD and FDTD methods, as the discontinuous Galerkin method allows discontinuous basis functions across different subdomains. Highly parallel discontinuous Galerkin time-domain methods have been recently employed for the solution of Maxwell's equations [13–20], but apparently this idea has not been used in the hybridization of the FETD method with FDTD method.

A new hybrid FDTD/FETD method is presented in this study. The FDTD grid and the FETD mesh can be quasi non-overlapping, i.e., they can have completely different meshes except that a buffer zone is needed to stitch them together. Furthermore, this scheme allows multiple FETD subdomains, an important feature for large-scale problems. In Section 2, we present the spatial discretization of the DG-FETD for this hybrid method. Section 3 demonstrates the coupling scheme between the FETD and FDTD methods. Numerical examples are given in Section 4 to show the validity of this method and its applications.

2 Formulation

We aim to solve for the electric and magnetic fields from Faraday's and Ampere's laws in Maxwell's equations. For the sake of simplicity without losing generality, only lossless media are considered here, although the implementation includes arbitrary conductivity losses:

$$\epsilon \frac{\partial \mathbf{E}}{\partial t} - \nabla \times \mathbf{H} = -\mathbf{J}, \tag{2.1a}$$

$$\mu \frac{\partial \mathbf{H}}{\partial t} + \nabla \times \mathbf{E} = 0, \qquad (2.1b)$$

where $\mathbf{E}$ and $\mathbf{H}$ are the time varying electric and magnetic fields; $\mathbf{J}$ represents the electric current density; ϵ and μ denote material's permittivity and permeability, respectively.

2.1 The overall scheme

As shown in Fig. 1, a complex structure is divided into several subdomains. The FDTD method is employed to simulate large and smoothly inhomogeneous media without complex structures; the FETD method is used for subdomains with complex geometries without causing substantial stair-casing errors as in the FDTD method. The interfaces between adjacent subdomains are in general non-conformal, i.e., the meshes on either sides of the interface can be unmatched.
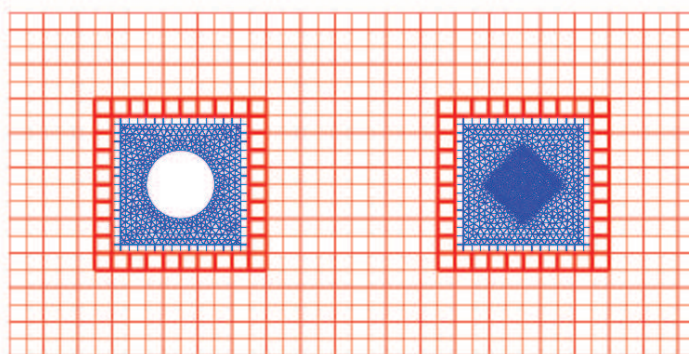

Figure 1: Domain decomposition with the FDTD and discontinuous Galerkin FETD methods. The FDTD method is used in a subdomain with a regular grid (the red region with a rectangular grid), while the DG-FETD method is used in subdomains with unstructured or structured meshes (blue triangular and blue rectangular regions) for complex geometry. A buffer zone (the heavy red rectangular elements) connects the FETD and FDTD subdomains. Shown here are two FETD subdomains with unstructured triangular meshes, two FETD subdomains with structured rectangular meshes and one FDTD subdomain.

2.2 The FDTD method

The FDTD method is the most popular and established method in time-domain simulation of electromagnetic waves. It was proposed by Yee in 1966 [1]. In this work we adopt the conventional FDTD scheme using central differences on a staggered Cartesian grid with a leap-frog scheme for the time integration. The detail will not be elaborated here due to the space limitation.

2.3 The DG-FETD method for the first-order PDEs

The discontinuous Galerkin FETD method is used for subdomains with complex structures. Denote $\mathbf{N}_e$ and $\mathbf{N}_h$ as basis/testing functions for $\mathbf{E}$ and $\mathbf{H}$, respectively. The corre-

sponding weak-forms of Maxwell's equations are

$$\int_{S_i}\left(\epsilon\mathbf{N}_e\cdot\frac{\partial\mathbf{E}}{\partial t}-\mathbf{N}_e\cdot\nabla\times\mathbf{H}+\mathbf{N}_e\cdot\mathbf{J}\right)ds=0, \tag{2.2a}$$

$$\int_{S_i}\left(\mu\mathbf{N}_h\cdot\frac{\partial\mathbf{H}}{\partial t}+\mathbf{N}_h\cdot\nabla\times\mathbf{E}\right)ds=0, \tag{2.2b}$$

where S_i denotes the area of the i-th subdomain. There can be one or more elements in a subdomain. Using integration by parts and the Gauss's theorem for the above equations and applying some simple identities, we obtain

$$\int_{S_i}\left(\epsilon\mathbf{N}_e\cdot\frac{\partial\mathbf{E}}{\partial t}+\mathbf{N}_e\cdot\mathbf{J}\right)ds=\int_{S_i}\nabla\times\mathbf{N}_e\cdot\mathbf{H}ds+\int_{L_i}\mathbf{N}_e\cdot(\hat{\mathbf{n}}\times\mathbf{H})dl, \tag{2.3a}$$

$$\int_{S_i}\mu\mathbf{N}_h\cdot\frac{\partial\mathbf{H}}{\partial t}ds=-\int_{S_i}\nabla\times\mathbf{N}_h\cdot\mathbf{E}ds-\int_{L_i}\mathbf{N}_h\cdot(\hat{\mathbf{n}}\times\mathbf{E})dl, \tag{2.3b}$$

where L_i denotes the subdomain surface, $\hat{\mathbf{n}}$ is the outward unit normal of the boundary. The interface relationship between fields in subdomain i and its neighbor subdomain can be evaluated as numerical fluxes $\hat{\mathbf{n}}\times\mathbf{E}$ and $\hat{\mathbf{n}}\times\mathbf{H}$. The two surface integral items $\int_{L_i}\mathbf{N}_e\cdot(\hat{\mathbf{n}}\times\mathbf{H})dl$ and $\int_{L_i}\mathbf{N}_h\cdot(\hat{\mathbf{n}}\times\mathbf{E})dl$ are over the interfaces between subdomains. In the DG-FETD method the basis functions $\mathbf{N}_e$ and $\mathbf{N}_h$ are not required to be continuous across interfaces between adjacent subdomains. So a non-conforming mesh can be utilized between subdomains. The Riemann solver (i.e., the upwind scheme) [21–23] is used here to calculate the above numerical fluxes. Take the i-th subdomain as the local subdomain and assume it is adjacent to the j-th subdomain. The corrected fields on the interface will be

$$\hat{\mathbf{n}}\times\mathbf{E}=\hat{\mathbf{n}}\times\frac{Y^{(i)}\mathbf{E}^{(i)}+Y^{(j)}\mathbf{E}^{(j)}}{Y^{(i)}+Y^{(j)}}-\hat{\mathbf{n}}\times\hat{\mathbf{n}}\times\frac{\mathbf{H}^{(i)}-\mathbf{H}^{(j)}}{Y^{(i)}+Y^{(j)}}, \tag{2.4a}$$

$$\hat{\mathbf{n}}\times\mathbf{H}=\hat{\mathbf{n}}\times\frac{Z^{(i)}\mathbf{H}^{(i)}+Z^{(j)}\mathbf{H}^{(j)}}{Z^{(i)}+Z^{(j)}}+\hat{\mathbf{n}}\times\hat{\mathbf{n}}\times\frac{\mathbf{E}^{(i)}-\mathbf{E}^{(j)}}{Z^{(i)}+Z^{(j)}}, \tag{2.4b}$$

where $\mathbf{E}^{(i)}$ and $\mathbf{H}^{(i)}$ are fields from the local (i-th) subdomain, $\mathbf{E}^{(j)}$ and $\mathbf{H}^{(j)}$ are from the neighbor (j-th) subdomain

$$Z^{(i)}=\frac{1}{Y^{(i)}}=\sqrt{\frac{\mu^{(i)}}{\epsilon^{(i)}}}, \tag{2.5a}$$

$$Z^{(j)}=\frac{1}{Y^{(j)}}=\sqrt{\frac{\mu^{(j)}}{\epsilon^{(j)}}}, \tag{2.5b}$$

Z and Y are wave impedance and admittance of the medium for the i-th subdomain and the j-th subdomain, respectively.

The discretized equations by the DG-FETD for the i-th subdomain are

$$\mathbf{M}_{ee}^{(i)}\frac{d\mathbf{e}^{(i)}}{dt}=\mathbf{K}_{ee}^{(i)}\mathbf{e}^{(i)}+\mathbf{K}_{eh}^{(i)}\mathbf{h}^{(i)}+\mathbf{f}^{(i)}+\sum_j\mathbf{L}_{ee}^{(ij)}\mathbf{e}^{(j)}+\sum_j\mathbf{L}_{eh}^{(ij)}\mathbf{h}^{(j)}, \tag{2.6a}$$

$$\mathbf{M}_{hh}^{(i)}\frac{d\mathbf{h}^{(i)}}{dt}=\mathbf{K}_{he}^{(i)}\mathbf{e}^{(i)}+\mathbf{K}_{hh}^{(i)}\mathbf{h}^{(i)}+\sum_j\mathbf{L}_{he}^{(ij)}\mathbf{e}^{(j)}+\sum_j\mathbf{L}_{hh}^{(ij)}\mathbf{h}^{(j)}, \tag{2.6b}$$

where $\mathbf{e}^{(i)}$ and $\mathbf{h}^{(i)}$ are vectors of the discretized electric and magnetic fields, $\mathbf{M}_{ee}^{(i)}$ and $\mathbf{M}_{hh}^{(i)}$ are the mass matrices, $\mathbf{K}_{ee}^{(i)}$, $\mathbf{K}_{hh}^{(i)}$, $\mathbf{K}_{eh}^{(i)}$ and $\mathbf{K}_{he}^{(i)}$ are the stiffness matrices and $\mathbf{f}^{(i)}$ is the discretized excitation vector in the i-th subdomain. These matrices and vectors are defined as

$$\left[\mathbf{M}_{ee}^{(i)}\right]_{mn}=\int_{S_i}\epsilon\mathbf{N}_{e_m}^{(i)}\cdot\mathbf{N}_{e_n}^{(i)}ds, \qquad\qquad \left[\mathbf{M}_{hh}^{(i)}\right]_{mn}=\int_{S_i}\mu\mathbf{N}_{h_m}^{(i)}\cdot\mathbf{N}_{h_n}^{(i)}ds, \tag{2.7a}$$

$$\left[\mathbf{K}_{ee}^{(i)}\right]_{mn}=\int_{L_i}\mathbf{N}_{e_m}^{(i)}\cdot\frac{\hat{\mathbf{n}}\times\hat{\mathbf{n}}\times\mathbf{N}_{e_n}^{(i)}}{Z^{(i)}+Z^{(j)}}dl, \qquad \left[\mathbf{K}_{hh}^{(i)}\right]_{mn}=\int_{L_i}\mathbf{N}_{h_m}^{(i)}\cdot\frac{\hat{\mathbf{n}}\times\hat{\mathbf{n}}\times\mathbf{N}_{h_n}^{(i)}}{Y^{(i)}+Y^{(j)}}dl, \tag{2.7b}$$

$$\left[\mathbf{K}_{eh}^{(i)}\right]=\int_{S_i}\nabla\times\mathbf{N}_{e_m}^{(i)}\cdot\mathbf{N}_{h_n}^{(i)}ds+\int_{L_i}\mathbf{N}_{e_m}^{(i)}\cdot\frac{\{\hat{\mathbf{n}}\times\mathbf{N}_{h_n}^{(i)}\}Z^{(i)}}{Z^{(i)}+Z^{(j)}}dl, \tag{2.7c}$$

$$\left[\mathbf{K}_{he}^{(i)}\right]_{mn}=-\int_{S_i}\nabla\times\mathbf{N}_{h_m}^{(i)}\cdot\mathbf{N}_{e_n}^{(i)}ds-\int_{L_i}\mathbf{N}_{h_m}^{(i)}\cdot\frac{\{\hat{\mathbf{n}}\times\mathbf{N}_{e_n}^{(i)}\}Y^{(i)}}{Y^{(i)}+Y^{(j)}}dl, \tag{2.7d}$$

$$\left[\mathbf{L}_{ee}^{(ij)}\right]_{mn}=-\int_{L_i}\mathbf{N}_{e_m}^{(i)}\cdot\frac{\hat{\mathbf{n}}\times\hat{\mathbf{n}}\times\mathbf{N}_{e_n}^{(j)}}{Z^{(i)}+Z^{(j)}}dl, \qquad \left[\mathbf{L}_{hh}^{(ij)}\right]_{mn}=-\int_{L_i}\mathbf{N}_{h_m}^{(i)}\cdot\frac{\hat{\mathbf{n}}\times\hat{\mathbf{n}}\times\mathbf{N}_{h_n}^{(j)}}{Y^{(i)}+Y^{(j)}}dl, \tag{2.7e}$$

$$\left[\mathbf{L}_{eh}^{(ij)}\right]_{mn}=\int_{L_i}\mathbf{N}_{e_m}^{(i)}\cdot\frac{\{\hat{\mathbf{n}}\times\mathbf{N}_{h_n}^{(j)}\}Z^{(j)}}{Z^{(i)}+Z^{(j)}}dl, \qquad \left[\mathbf{L}_{he}^{(ij)}\right]_{mn}=-\int_{L_i}\mathbf{N}_{h_m}^{(i)}\cdot\frac{\{\hat{\mathbf{n}}\times\mathbf{N}_{e_n}^{(j)}\}Y^{(j)}}{Y^{(i)}+Y^{(j)}}dl, \tag{2.7f}$$

$$\left[\mathbf{f}^{(i)}\right]_m=-\int_{S_i}\mathbf{N}_{e_m}^{(i)}\cdot\mathbf{J}ds. \tag{2.7g}$$

The matrices $\mathbf{L}_{ee}^{(ij)}$, $\mathbf{L}_{eh}^{(ij)}$, $\mathbf{L}_{he}^{(ij)}$ and $\mathbf{L}_{hh}^{(ij)}$ are obtained from the boundary integrals over the interface between the i-th subdomain and the j-th subdomain and they can be viewed as the coupling matrices between the local subdomain and its neighboring subdomains. In general, they are very sparse matrices. All the detailed formulations of the above matrices and vectors can be referred to [12] and [24–26].

Following the spatial discretization, we obtain Eqs. (2.6a) and (2.6b) for i-th subdomain. Then we can obtain similar equations for other subdomains with similar explanations. These equations constitute an ordinary differential (ODE) system with only time derivatives.

By employing the discontinuous Galerkin technique, a large global mass matrix is therefore replaced by a set of smaller mass matrices corresponding to each subdomain,

which are much easier to be inverted or factorized. Several different time-stepping methods can be used for the discretized system (2.6a) and (2.6b) based on the properties of each subdomain. For example, an explicit scheme such as the 4th-order Runge-Kutta method (RK4) can be used for subdomains with relatively coarse meshes. While the largest time step by RK4 is generally determined by the spectrum of the discretized system by DG-FETD, which may call some expensive eigensolver, we found an empirical stability criterion for DG-FETD method with RK4 time stepping scheme as:

$$\Delta t_{\text{DG-FETD}} \leq \left(\frac{\sqrt{3}}{4} \frac{h_{\min}}{c} \right), \tag{2.8}$$

where $h_{\min}$ denotes the shortest edge among the DG-FETD meshes of all subdomains and c denotes the speed of light.

So the stability limit of the time step in the hybrid FDTD/FETD method will be

$$\Delta t \leq \min \left\{ \Delta t_{\text{FDTD}}, \Delta t_{\text{DG-FETD}} \right\}, \tag{2.9}$$

where Δt_{FDTD} denotes the well-established stability criterion for the FDTD method.

2.4   Coupling between the DG-FETD and FDTD methods

For the example of 2-D TM$_z$ case in Fig. 2, the edges (H_x, H_y) in FDTD subdomains of the rectangular Yee's grid are updated using the traditional FDTD scheme. Thereafter, the edges marked by crosses in Fig. 2 are exported from the rectangular FDTD grid to the FETD mesh. This provides the discretized system of Eqs. (2.6a) and (2.6b) with a Dirichlet boundary condition:

$$\mathbf{h}^{(i)} = \mathbf{h}_{\Gamma}^{\text{FE}}, \quad \text{on} \ \ \Gamma_{\text{FE}}^{(i)}, \tag{2.10}$$

where $\Gamma_{\text{FE}}^{(i)}$ denotes the boundary of $\Omega_{\text{FE}}^{(i)}$ between the FETD and FDTD subdomains (i.e., all the edges marked by crosses in Fig. 2).

During the RK4 time integration in the FETD subdomains, at each sub-step, the solution associated with the edges marked by circles (H_x and H_y in the FDTD subdomain) in Fig. 2 is exported to the explicit FETD grid as the known field values. Then the updated magnetic field at the circles in Fig. 2 is used to calculate the electric and magnetic fields at the next time steps. This completes one cycle in the time stepping scheme and the FDTD scheme can again be applied to update the fields. Specifically, let us assume that the fields

$$\mathbf{E}^{n-\frac{1}{2}} = \hat{z} E_z^{n-\frac{1}{2}},$$

and

$$\mathbf{H}^n = \hat{x} H_x^n + \hat{y} H_y^n,$$

are known in the FDTD grid and $\mathbf{E}^{n-1/2}$ and $\mathbf{H}^n$ are known on the FETD mesh, where the superscripts denote the time step index. To advance the fields to the next time step, we use the following procedures:
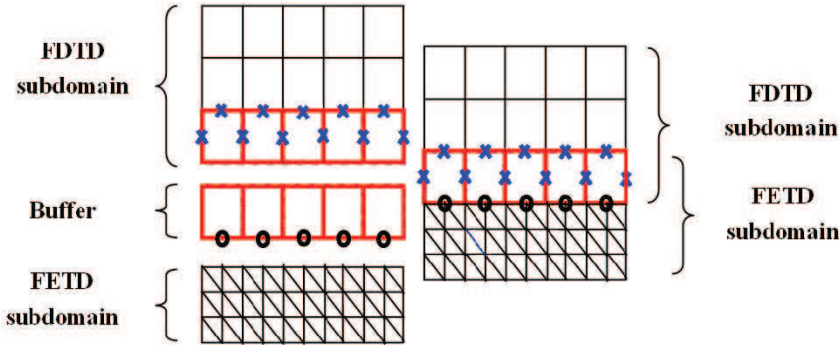
Figure 2: Unknowns associated with edges marked by crosses, $\mathbf{H}_{FD}$ in the TM$_z$ case, are exported from the FDTD grid to the FETD mesh; and those marked by circles, $\mathbf{H}_{FE}$, are exported from the FETD mesh to the FDTD grid. The TE$_z$ case is dual to this configuration and is not shown here.

1. Use the FDTD method to advance the electric field to $\mathbf{E}^{n+1/2}$ using the known $\mathbf{E}^{n-1/2}$ and $\mathbf{H}^n$ in the FDTD grid in Fig. 2.

2. Use the FDTD method to advance the magnetic field to $\mathbf{H}^{n+1}$ using the known $\mathbf{H}^n$ and $\mathbf{E}^{n+1/2}$ in the FDTD grid in Fig. 2.

3. Pass $\mathbf{H}_{\mathrm{FD}}^{n+1}$ components, marked by crosses in Fig. 2, from the FDTD grid to the FETD buffer zone as the boundary values. Together with $\mathbf{H}_{\mathrm{FD}}^n$ at the previous step, one can calculate these boundary values

$$\mathbf{H}_{\mathrm{FD}}^{n+\frac{1}{2}} = \frac{\mathbf{H}_{\mathrm{FD}}^n + \mathbf{H}_{\mathrm{FD}}^{n+1}}{2},$$

by simple linear interpolation. These known boundary values are denoted as $\tilde{\mathbf{y}}_b^n$ and $\tilde{\mathbf{y}}_b^{n+1/2}$, respectively.

4. Use the RK4 time integration method to advance the fields in the FETD subdomain from n-th time step to $(n+1)$-th time step. We denote all the unknown fields in all subdomains by $\mathbf{y} = [\tilde{\mathbf{y}}_b, \mathbf{y}_i]^T$, where $\mathbf{y}_i$ denotes the fields other than those given by the known boundary values in Step 3 above. The system in Eq. (2.7a) can be written as

$$\frac{d\mathbf{y}}{dt} = \mathbf{A}\mathbf{y} + \mathbf{s},$$

where $\mathbf{A}$ is a matrix and $\mathbf{s}$ is an excitation. Then by the RK4 scheme, we have

$$\mathbf{y}^{n+1} = \mathbf{y}^n + \frac{\Delta t}{6}(\mathbf{k}_1 + 2\mathbf{k}_2 + 2\mathbf{k}_3 + \mathbf{k}_4), \tag{2.11}$$

where

$$\mathbf{k}_1 = \mathbf{A}\begin{bmatrix} \tilde{\mathbf{y}}_b^n \\ \mathbf{y}_i^n \end{bmatrix} + \mathbf{s}^n, \qquad \mathbf{k}_2 = \mathbf{A}\begin{bmatrix} \tilde{\mathbf{y}}_b^{n+\frac{1}{2}} \\ \mathbf{y}_i^n + \frac{\Delta t}{2}\mathbf{k}_{1,i} \end{bmatrix} + \mathbf{s}^{n+\frac{1}{2}}, \tag{2.12a}$$

$$\mathbf{k}_3 = \mathbf{A}\begin{bmatrix} \tilde{\mathbf{y}}_b^{n+\frac{1}{2}} \\ \mathbf{y}_i^n + \frac{\Delta t}{2}\mathbf{k}_{2,i} \end{bmatrix} + \mathbf{s}^{n+\frac{1}{2}}, \qquad \mathbf{k}_4 = \mathbf{A}\begin{bmatrix} \tilde{\mathbf{y}}_b^{n+1} \\ \mathbf{y}_i^n + \Delta t\mathbf{k}_{3,i} \end{bmatrix} + \mathbf{s}^{n+1}, \tag{2.12b}$$

and $\mathbf{k}_{j,i}$ denotes the interior components of the $\mathbf{k}_j$ $(j=1,2,3,4)$ vectors, similar to the definition of $\mathbf{y}_i$. After this RK4 time integration for one full time step, the magnetic field values at the circles in Fig. 2, denoted by $\mathbf{H}_{\mathrm{FE}}^{n+1}$ are known together with the other field values in the FETD subdomains.

5. Pass $\mathbf{H}_{\text{FE}}^{n+1}$ to the FDTD subdomain so that the fields in the whole FDTD subdomain are now known for the $(n+1)$-th time step.

6. Go to Step 1 and repeat the process until the specified length of time window has been reached.

The above hybrid scheme has been implemented for two-dimensional TM_z and TE_z problems and has been validated and applied as shown in the following section.

3   Numerical examples and discussions

3.1   Plane wave incident in open area

The first example is to simulate the propagation of a plane wave in open area. The computational domain a 7.2 m × 0.9 m rectangular area. The time-varying form of the plane wave is a Gaussian pulse:

$$\mathbf{E}^{(i)} = \exp\left[-\frac{4\pi(t-1.6\times10^{-9})^2}{(5.0\times10^{-9})^2}\right]. \tag{3.1}$$

We test this example with the hybrid FDTD/FETD with different discretization density and use the results by FDTD with a very fine grid as the reference. Fig. 3 shows the relative error versus the sampling density in terms of the number of points per wavelength (PPW), from which we can see that the hybrid FDTD/FETD method approximately has a second order accuracy.
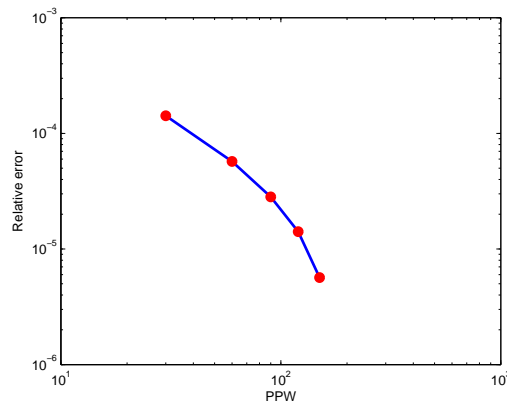

Figure 3: The L_2 relative error versus the sampling density in terms of the number of points per wavelength (PPW) for a plane wave incident in an open area.

3.2   A cylinder in a rectangular cavity

This example is a circular cylinder inside a rectangular cavity. As shown in Fig. 4, the size of the rectangular cavity is 0.8 m × 1.0 m and the circular cylinder of radius 0.1
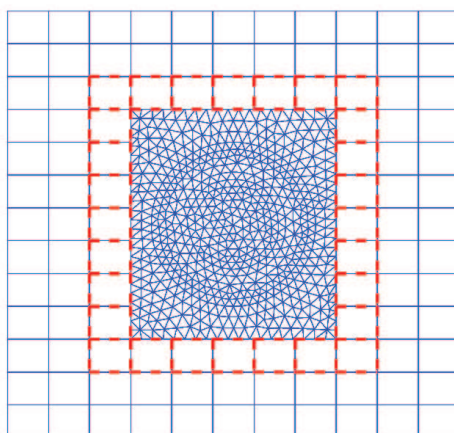
Figure 4: A nonconforming mesh for the hybrid FETD-FDTD modeling of a circular cylinder in a 0.8 m ×1.0 m rectangular cavity. Cells marked by heavy dashed lines are in the buffer zone between the FETD and FDTD subdomains.

m is co-centered with the rectangular cavity. The circular cylinder is discretized by an unstructured triangular mesh. The region with triangular elements is contained in a box of 5 × 7 FDTD cells; the buffer zone (head red dashed lines) contains 28 FDTD cells (also exactly 28 FETD rectangular elements). The rest of the cavity is discretized by 20 × 20 FDTD cells. The outer boundary of the cavity is set as PEC.

First, the circular cylinder is set as air, the same material as the rest of the cavity. We use the $\Delta t = h_{\min}/(4c)$ and test the stability by taking 500000 time steps. No instability issues has been found.

The resonance frequencies of this cavity is calculated by discrete Fourier transform of the time-varying E_z fields and listed in Table 1. Good agreement is found between numerical and analytical solutions.

Table 1: Eigenvalues from the hybrid FDTD/FETD method for a rectangular cavity of dimensions 0.8 m ×1.0 m with air.

Mode	Numerical [GHz]	Exact [GHz]	Error [%]
TM11	0.242	0.240	0.96
TM21	0.354	0.354	0.00
TM12	0.403	0.404	0.13
TM31	0.479	0.480	0.31
TM22	0.491	0.487	0.85
TM32	0.582	0.582	0.03

We also set the cylinder as a dielectric one with relative permittivity equal to 4. Table 2 shows good agreement between numerical results of the resonant frequencies by the hybrid FDTD/FETD and reference results by FEM with a very dense mesh.

Table 2: Eigenvalues of the rectangular cavity (0.8 m $\times$ 1.0 m) with a circular dielectric cylinder ($\epsilon_r = 4$) from hybrid FDTD/FETD and FETD methods.

Mode number	Numerical [GHz]	FEM [GHz]	Error [%]
1	0.195	0.194	0.68
2	0.344	0.344	0.00
3	0.387	0.387	0.05
4	0.412	0.413	0.12
5	0.477	0.480	0.66
6	0.541	0.546	0.90

3.3 A dielectric in an open area

As shown in Fig. 5, a square dielectric cylinder with side length equal to 0.225 m is placed in an unbounded area. Here and in following cases the unbounded medium is truncated by applying a perfectly matched layer (PML) absorbing boundary condition. The origin of the coordinate system is placed at the center of the dielectric. The positive x and y axes both coincide with the diagonal lines of the dielectric cylinder. The dielectric constant of this cylinder is set as $\epsilon_r = 16$. A Blackman-Harris window (BHW) pulse [14, 27] is used as the source located at (-0.35353, 0) m. The receiver is located at (0.35353, 0) m.
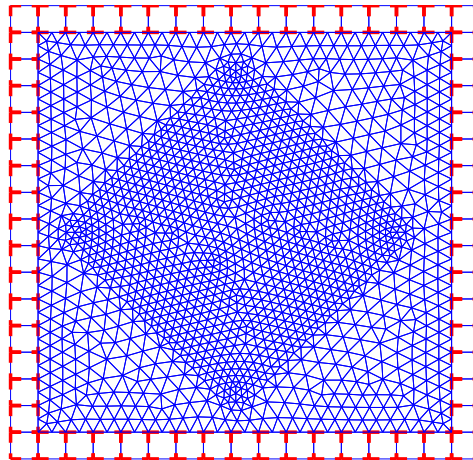

Figure 5: A dielectric square with $\epsilon_r = 16$ in an open space. Cells marked by heavy dashed lines are in the buffer zone between the FETD and FDTD subdomains, but the uniform FDTD grid outside the buffer zone is not shown here for clarity.

We carry out the time integration for 8000 steps by the proposed hybrid FDTD/FETD scheme with $\Delta t = h_{\min}/(4c)$. We use calculated results by FDTD with a relatively fine grid as the reference. In the reference FDTD solution, the model of the dielectric cylinder is rotated 45° so that the square is aligned with coordinate axes to remove the substan-
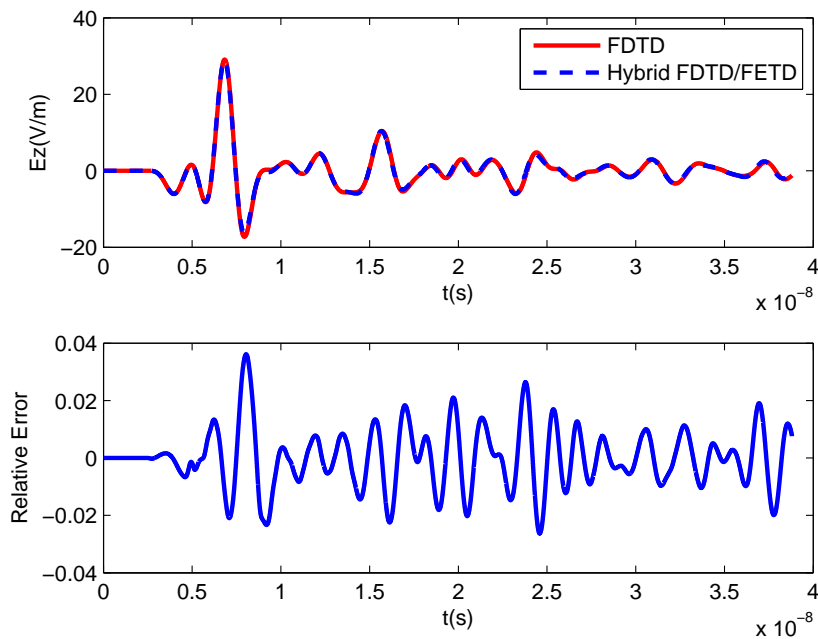
Figure 6: Comparison of the E_z result from the hybrid FETD-FDTD method and that from the FDTD with a very fine grid for the problem in Fig. 5. Top: The E_z component versus time. Bottom: The relative error of the hybrid result (normalized by the peak value of E_z).

tial stair-casing errors in the conventional FDTD method. Fig. 6 shows the comparison between numerical results by the hybrid FDTD/FETD method and the reference results, from which we can clearly see that these two results agree well.

3.4   Two PEC strips in an open area

Fig. 7 shows two PEC strips with a 90° corner in an unbounded domain. We use three subdomains in this problem: one subdomain uses triangular elements for the region surrounding the strips; the second subdomain uses rectangular elements for the buffer zone; and last subdomain is the FDTD grid used in the outermost region. It is a nonconforming mesh between the rectangular mesh and the buffer zone. An electric dipole line source with the BHW pulse marked as an arrow is placed between the strips at the upper left corner. The receiver is placed at the other end of the strips. This case is therefore a TE_z case with the electric field perpendicular to the z axis.

We carry out the time integration for 8000 steps by the proposed hybrid FDTD/FETD scheme with a denser mesh and a coarser mesh as shown in Fig. 7. Fig. 8 shows the numerical results by the proposed hybrid FDTD/FETD with a denser mesh and a coarser mesh, from which we can clearly see that these two results are reasonable.
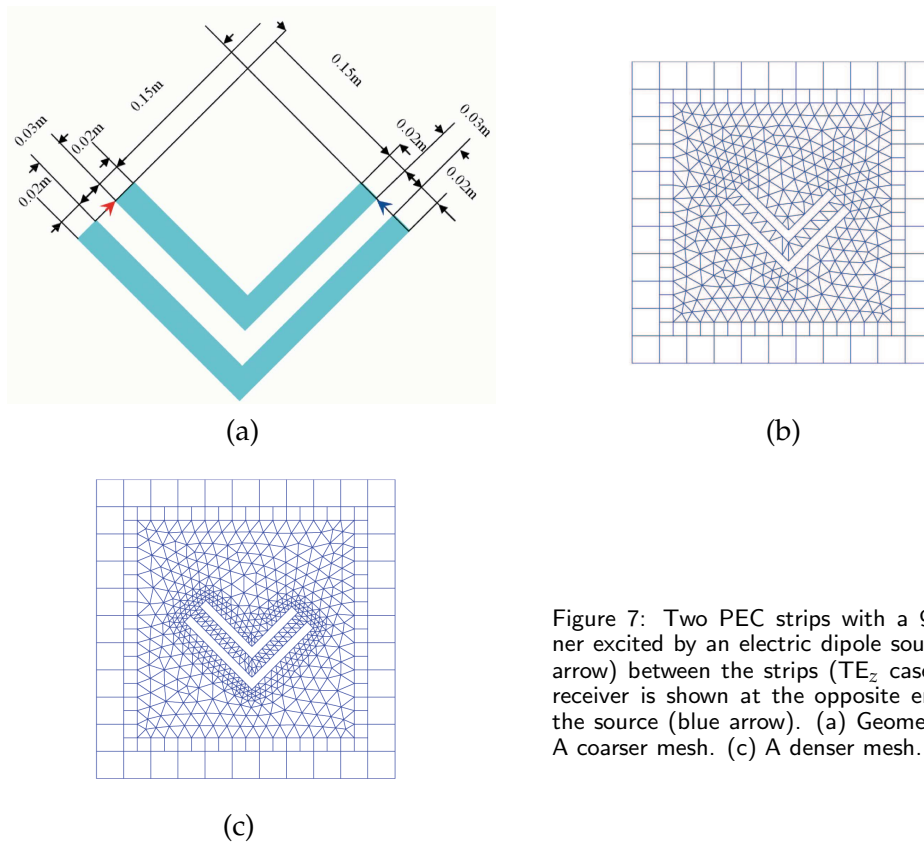
(a)

(b)

(c)

Figure 7: Two PEC strips with a 90° corner excited by an electric dipole source (red arrow) between the strips (TE$_z$ case). The receiver is shown at the opposite end from the source (blue arrow). (a) Geometry. (b) A coarser mesh. (c) A denser mesh.
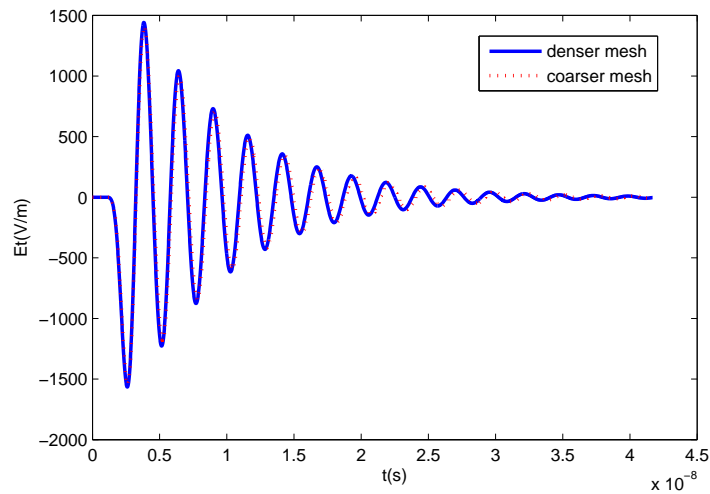

Figure 8: Transverse electric field component E_t versus time at the end of the strips in Fig. 7 as calculated by a coarser mesh and by a denser mesh.
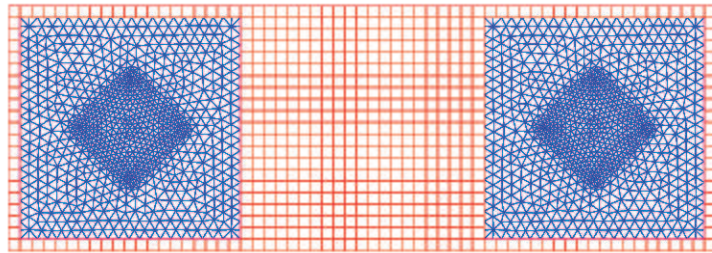
Figure 9: Part of the mesh for the hybrid FDTD/FETD method for two dielectric square cylinders ($\epsilon_r = 4$) in an unbounded region. Triangular elements are used in two FETD subdomains to model the tilted dielectric cylinders, while a rectangular grid is used in the FDTD region for the homogeneous area.

3.5   Two dielectrics in an open area

As shown in Fig. 9, two square dielectric cylinders ($\epsilon_r = 4$) with side length 0.25 m are both rotated at a 45° angle with respect to the x axis and placed side by side in an unbounded domain. The centers of the two dielectrics are located at $(-\sqrt{2}, 0)$ and $(\sqrt{2}, 0)$ m, respectively. The outer boundary is modeled as an absorbing boundary condition through the perfectly matched layer (PML). The computational domain is meshed by an FDTD region outside ($\Delta x = 0.0354$, $\Delta y = 0.0354$ m), while the two square dielectric cylinders are discretized by two triangular FETD meshes. The FETD buffer zones with one cell thick surrounding the FETD subdomains coincide with the FDTD grid. The FETD meshes are non-conformal to the outer FDTD grid. An electric line source with the BHW
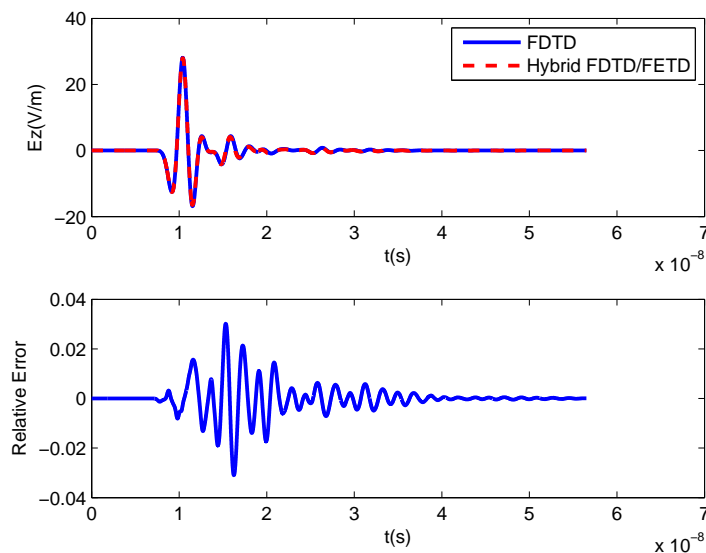

Figure 10: Comparison of the results from the hybrid FETD-FDTD method and from the reference FDTD solution with a fine grid for the problem in Fig. 9. Top: E_z versus time. Bottom: Relative difference normalized by the peak value of E_z.

pulse is located at $(-3\sqrt{2}/2, 0)$ m, while the receiver is located at $(3\sqrt{2}/2, 0)$ m.

We carry out the time integration for 8000 steps by the proposed hybrid FDTD/FETD scheme with $\Delta t = 3.5236$ ps for this TE_z case. The numerical result for E_z is shown in Fig. 10. For comparison we also plot the reference numerical result by the FDTD method with a much finer grid. From this figure we observe that the two results agree well.

4   Conclusions

We propose a new hybrid scheme to combine the finite difference time-domain method and finite element time method for transient electromagnetic simulations. This method allows multiple FETD subdomains and the mesh can be arbitrary non-conformal between different subdomains. Thus, the mesh in the proposed method can be flexible and efficient for a large number of realistic problems and it is much easier for meshing during preprocessing than the conventional FDTD method or FETD method because different subdomains can be meshed independently. By dividing a large domain into several smaller subdomains the proposed method can solve much larger problems than the conventional FETD methods without sacrificing accuracy. To the best of our knowledge, this is a new method in the hybridization of FDTD and FETD methods for multiscale electromagnetic simulations. Numerical examples demonstrate the effectiveness of this method.

References

[1] K. Yee, Numerical solution of initial boundary value problems involving Maxwell's equations in isotropic media, IEEE Trans. Antennas. Propag., 14 (1966), 302–307.

[2] J. F. Lee and Z. Sacks, Whitney elements time domain (WETD) methods, IEEE Trans. Magn., 31 (1995), 1325–1329.

[3] R. Wu and T. Itoh, Hybridizing FD-TD analysis with unconditionally stable FEM for objects of curved boundary, IEEE MTT-S., 2 (1995), 833–836.

[4] E. Abenius, U. Andersson and L. Edlvik, Hybrid time domain solvers for the Maxwell equations in 2D, Int. J. Numer. Methods. Eng., 53 (2002), 2185–2199.

[5] T. Rylander and A. Bondeson, Stability of explicit-implicit hybrid time step scheme for Maxwell equations, J. Comput. Phys., 14 (2002), 426–438.

[6] N. V. Venkatarayalu, Y. B. Gan and L. W. Li, Investigation of numerical stability of 2D FE/FDTD hybrid algorithm for different hybridization scheme, IEICE. Trans. Commun., E88-B (2005), 2314–2345.

[7] N. V. Venkatarayalu, Y. B. Gan and L. W. Li, On the numerical errors in the 2D FE/FDTD algorithm for different hybridization schemes, IEEE Microw. Wirel. Co., 14 (2004), 168–170.

[8] N. V. Venkatarayalu, R. Lee, Y. B. Gan and L. W. Li, A stable FDTD subgridding method based on finite element formulation with hanging variables, IEEE Trans. Antennas. Propag., 55 (2007), 907–915.

[9] W. D. Guo, G. H. Shiue, C. M. Lin and R. B. Wu, An integrated signal and power integrity analysis for signal traces through the parallel planes using hybrid finite-element and finite-difference time-domain techniques, IEEE T. Adv. Packaging., 30 (2007), 558–565.

[10] J. F. Lee, R. Lee and A. Cangellaris, Time-domain finite-element methods, IEEE Trans. Antennas. Propag., 45 (1997), 430–441.

[11] J. L. Coulomb, F. X. Zgainski and Y. Marechal, A pyramidal element to link hexahedral, prismatic and tetrahedral edge finite elements, IEEE Trans. Magnetics., 33 (1997), 1362–1365.

[12] J. H. Lee, J. Chen and Q. H. Liu, A 3-D discontinuous spectral element time-domain method for Maxwell's equations, IEEE Trans. Antennas. Propag., 57 (2009), 2666–2674.

[13] T. Xian and Q. H. Liu, Three-dimensional unstructured-grid discontinuous Galerkin method for Maxwell's equations with well-posed perfectly matched layer, Microw. Opt. Techn. Let., 46 (2005), 459–463.

[14] Q. H. Liu and G. Zhao, Advances in PSTD Techniques, Chapter 17, Computational Electromagnetics: The Finite-Difference Time-Domain Method, A. Taflove and S. Hagness, Artech House, Inc., 2005.

[15] J. S. Hesthaven and T. Warburton, Nodal high-order methods on unstructured grids-I: time-domain solution of Maxwell's equations, J. Comput. Phys., 181 (2002), 186–211.

[16] J. S. Hesthaven and T. Warburton, High-order accurate methods for time-domain electromagnetics, Cmes-Comp. Model. Eng., 5 (2004), 395–407.

[17] D. Kopriva, S. Woodruff and M. Hussaini, Computation of electromagnetic scattering with a non-conforming discontinuous spectral element method, Int. J. Numer. Meth. Eng., 53 (2001), 105–122.

[18] B. Cockburn, F. Li and C. W. Shu, Locally divergence-free discontinuous Galerkin methods for the Maxwell equations, J. Comput. Phys., 194 (2004), 588–610.

[19] G. Cohen, X. Ferrieres and S. Pernet, A spatial high-order hexahedral discontinuous Galerkin method to solve Maxwell's equations in time domain, J. Comput. Phys., 217 (2006), 340–363.

[20] S. Gedney, C. Luo, J. Roden, R. Crawford, B. Guernsey, J. Miller, T. Kramer and E. W. Lucas, The discontinuous Galerkin finite-element time-domain method of Maxwell's equations, ACES J., 24 (2009), 129–142.

[21] A. H. Mohammadian, V. Shankar and W. F. Hall, Computation of electromagnetic scattering and radiation using a time-domain finite-volume discretization procedure, Comput. Phys. Commun., 68 (1991), 175–196.

[22] T. Lu, P. Zhang and W. Cai, Discontinuous Galerkin methods for dispersive and lossy Maxwell equations and PML boundary conditions, J. Comput. Phys., 200 (2004), 549–580.

[23] T. Lu, W Cai and P. Zhang, Discontinuous Galerkin time-domain method for GPR simulation in dispersive media, IEEE Trans. Geosci. Remote. Sensing., 43 (2005), 72–80.

[24] J. H. Lee and Q. H. Liu, A 3-D spectral-element time-domain method for electromagnetic simulation, IEEE Microw. Theory. Tech., 55 (2007), 983–991.

[25] J. Chen and Q. H. Liu, A non-spurious vector spectral element method for Maxwell's equations, Pr. Electromagn. Res. S., 96 (2009), 205–215.

[26] J. Chen, Q. H. Liu, M. Chai and J. A. Mix, A non-spurious 3-D vector discontinuous Galerkin finite-element time-domain method, IEEE Microw. Wirel. Co., 20(1) (2010), 1–3.

[27] Q. H. Liu, The PSTD algorithm: a time-domain method requiring only two cells per wavelength, Microw. Opt. Techn. Let., 15 (1997), 158–165.

[28] S. Gottlieb and L.-A. J. Gottlieb, Strong stability preserving properties of Runge-Kutta time discretization methods for linear constant coefficient operators, J. Sci. Comput., 18(1) (2003), 83–109.